Rare Met. (2022) 41(10):3504–3514
https://doi.org/10.1007/s12598-022-02038-6

RARE METALS

ORIGINAL ARTICLE

Microstructure and mechanical property of NbTaTiV refractory high-entropy alloy with different Y_2O_3 contents

Tao Liao, Yuan-Kui Cao*, Wen-Min Guo, Qi-Hong Fang, Jia Li, Bin Liu*

Received: 9 December 2021 / Revised: 12 January 2022 / Accepted: 15 January 2022 / Published online: 20 July 2022

Abstract In this study, NbTaTiV refractory high-entropy alloys (RHEAs) reinforced with dispersed oxides were successfully designed and fabricated by mechanical alloying and subsequent spark plasma sintering (SPS). The effects of Y_2O_3 content on the microstructure and mechanical properties have been systematically studied. The results show that the oxide dispersion strengthening (ODS) RHEAs are mainly composed of body centered cubic (BCC) matrix and multiscale oxides, including submicron Ti-(N, O) particles, nano-sized Y-Ti-O particles and nano-sized Y_2O_3 particles. The ODS-RHEAs have excellent mechanical properties due to the multiscale oxides. With the content of Y_2O_3 increasing from 1 wt% to 3 wt% Y_2O_3, the compressive yield strength of the ODS-RHEAs significantly increases from 1528 to 1866 MPa, while the fracture strain slightly reduces from 22% to 16%. The enhancement of the mechanical property is mainly attributed to the increased amount of multiscale oxide particles and the refined grain structure.

Keywords Refractory high-entropy alloy; Oxide dispersion strengthening; Spark plasma sintering (SPS); Mechanical property; Strengthening mechanism

T. Liao, Y.-K. Cao*, W.-M. Guo, B. Liu*
State Key Laboratory of Powder Metallurgy, Central South University, Changsha 410083, China
e-mail: caoyuankui@csu.edu.cn

B. Liu
e-mail: binliu@csu.edu.cn

Q.-H. Fang, J. Li
State Key Laboratory of Advanced Design and Manufacturing for Vehicle Body, Hunan University, Changsha 410082, China

1 Introduction

High-entropy alloys (HEAs) with equal or near-equal atomic ratios usually have supersaturated solid solutions, which can cause severe lattice distortion and thus enhance the mechanical properties of the alloy [1]. Based on the concept of HEAs, Senkov et al. [2] proposed refractory high-entropy alloys (RHEAs) that consisted of elements mainly from the IV–VI group and presented excellent high-temperature properties. For example, MoNbTaVW RHEA maintains a yield strength of 477 MPa at 1600 °C, which is significantly higher than that of traditional nickel-based super-alloys [3]. However, due to the presence of heavy elements such as W, Mo and Ta, these RHEAs have the problems of high density and high brittleness at room temperature. As an improvement, a series of plastic RHEAs based on lighter refractory elements such as Hf, Nb, Ti, V and Zr have been developed [4–7]. For example, NbTaTiV alloy exhibits excellent compressive plasticity (> 50%) at room temperature; however, its strength is slightly insufficient compared with that of RHEAs containing W and Mo, which needs to be further enhanced [5].

So far, researchers have tried a variety of methods, such as adding alloying elements or introducing ceramic particles, to improve the strength of the ductile NbTaTiV RHEAs. For example, HfNbTaTiV [6] and MoNbTaTiV [7] RHEAs exhibit yield strength of 1350 and 1400 MPa, respectively, which are remarkable higher than that of NbTaTiV alloy (~ 965 MPa) and still maintain good plasticity. However, the expensive elements Hf and Mo will limit their application. By utilizing the powder metallurgy method, a NbTaTiV composite reinforced with in situ formed Ti-C-O ceramic particles has been prepared in our previous work [8]; it shows excellent room-temperature and high-temperature strength, but also had the

problem of room-temperature brittleness (its room-temperature plasticity is even less than 5%). Therefore, it is important to find a new method to improve the strength of ductile RHEAs while maintaining their plasticity.

The beneficial effects of oxide dispersion strengthening in improving strength have been confirmed and utilized in many alloys, such as oxide dispersion strengthening (ODS)-Fe-based alloy and ODS-HEAs [9–12]. This method is mainly by adding fine oxide particles (Y_2O_3, Al_2O_3, etc.) to the matrix alloy. These oxide particles can either dispersively distribute in the matrix or react with the matrix to in situ generate ultra-fine oxide particles, thus hindering the movement of dislocations and the growth of grains, and thereby improving the mechanical properties [13–15]. For example, Gwalani et al. [9] prepared an ODS-$Al_{0.3}$CoCrFeMnNi HEA and found that the strength increased from 980 (0 vol% Y_2O_3) to 1760 MPa (3 vol% Y_2O_3) with a reasonable reduction in plasticity due to the dislocation pinning effects from the dispersive nano-oxides. Hadraba et al. [16] prepared an ODS-CoCrFeMnNi HEA and demonstrated that the yield strength of the ODS-HEA increased by 30% at room temperature and 70% at 800 °C due to the presence of dispersive in-situ nano-oxides. Although some previous works confirmed the strengthening effect of the dispersive oxides in HEAs, the ODS method is rarely reported in RHEAs.

Recently, an interesting phenomenon was reported in the NbTaTiV RHEA: when the alloy is prepared by ball milling and spark plasma sintering (SPS), the high content of O and N will react with Ti and produce dispersed submicron Ti-(N, O) particles, thereby improving the hardness and strength of the alloy [17]. Similar precipitation behavior has also been found in MoNbTaTiV [18] and Ti_xVNbMoTa [19] RHEAs. In view of the advantages of dispersed oxides on improving the mechanical properties, we designed a new multiscale ODS-NbTaTiV RHEA. In this RHEA, nano-sized Y_2O_3 particles were added to the NbTaTiV alloy by ball milling and spark plasma sintering method. On the one hand, adding Y and O will react with Ti to form nanoscale Y–Ti–O clusters during the ball milling, and the oxide clusters continue to nucleate and grow during the sintering process [11, 20, 21]. On the other hand, Ti has a strong affinity with O atoms decomposed from Y_2O_3 and N atoms from the residual air, and the reaction between them promotes the formation of Ti-(N, O) particles through repeated fracture and cold welding during the ball milling, which are gradually refined and dispersed in the matrix [18], thereby producing multiscale oxides structure, which may also help to improve the mechanical properties of NbTaTiV RHEAs.

In this study, ODS-NbTaTiV RHEAs were prepared by powder metallurgy (mechanical alloying (MA) + SPS), and the influences of Y_2O_3 content on the phase composition, microstructure and mechanical properties were systematically studied. The corresponding strengthening mechanisms were also discussed. This work aims to provide a new strategy for further improving the mechanical property of the ductile RHEAs.

2 Experimental

High-purity Nb, Ta, Ti and V powders (particle sizes < 45 μm, purity > 99.5 wt%) and Y_2O_3 powder (particle size of 30–50 nm, purity > 99 wt%) were used to prepare the ODS-NbTaTiV RHEAs. Three RHEAs with Y_2O_3 contents of 1 wt%, 2 wt% and 3 wt% were prepared. The powders were milled in a planetary ball mill (MITR-YXQM-4L) with a ball-to-powder mass ratio of 10:1 at 250 $r{\cdot}min^{-1}$ for 20 h. Tungsten carbide vials and balls were utilized as the milling media. The as-milled powders were sintered at a temperature of 1500 °C and a pressure of 40 MPa for 10 min using a spark plasma system (SPS, LABOX-325R).

Phase analysis was conducted in an X-ray diffractometer (XRD, D/MAX-2250) with Cu Kα radiation in 2θ range from 20° to 90°. The microstructural characteristics were performed in a field emission scanning electron microscope (FESEM, Quanta 650 FEG) equipped with an energy-dispersive X-ray spectroscopy (EDS) and a backscatter electron (BSE) detector. The detailed microstructure and the nano-sized particles were analyzed by using a transmission electron microscope (TEM, FEI Titan G2). The sample for TEM tests was prepared by iron thinning. Compression tests were proceeded on an Instron 8802 testing machine at room temperature, and all compression tests were performed at a strain rate of 1×10^{-3} s^{-1}. The samples used for the compression test have a cylindrical shape of Φ6 mm × 9 mm. The micro-hardness of the bulk alloys was measured by using a micro-hardness tester (MicroMet-5104 Vickers). The indenter load was 49 N (5 kg), and the pressure holding time was 20 s.

3 Results and discussion

3.1 As-milled powders

Figure 1 shows SEM images and XRD patterns of the as-milled powders with different Y_2O_3 contents. It can be seen that the powders are mainly nearly ellipsoidal, with a rough surface and obvious welding traces. The average particle size of the ball-milled powders with 1 wt% Y_2O_3, 2 wt% Y_2O_3 and 3 wt% Y_2O_3 is 15.18, 11.52 and 7.93 μm, respectively. The decrease in the average particle size of the powders is maybe due to the smashing effect of the

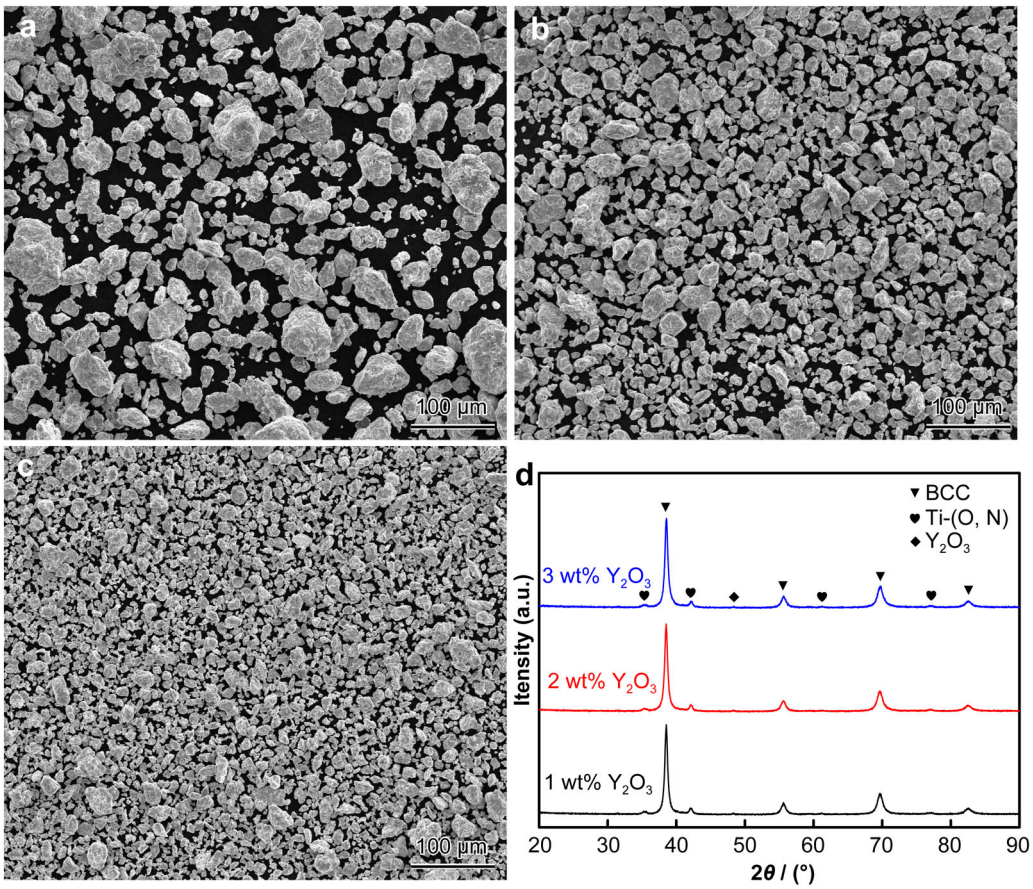

Fig. 1 **a–c** SEM images and **d** XRD patterns of as-milled powders of NbTaTiV RHEAs with different contents of Y_2O_3: **a** 1 wt% Y_2O_3; **b** 2 wt% Y_2O_3; **c** 3 wt% Y_2O_3

brittle Y_2O_3 particles, which could inhibit the cold welding and clustering of the raw powders. XRD results show that the powders are mainly composed of BCC phase (matrix) and face centered cubic (FCC) phase (precipitates). FCC phase could be Ti-(N, O) compound, which may come from the reaction between Ti and O or N atoms during milling, and it has also been reported in MoNbTaTiV alloy [18, 19]. With Y_2O_3 content increasing to 3 wt%, some diffraction peaks of Y_2O_3 appears, indicating that the amount of the Y_2O_3 is too much and can not be completely dissolved during the ball milling process.

3.2 Effect of Y_2O_3 content on microstructure

Figure 2 shows BSE images and XRD patterns of the bulk NbTaTiV RHEAs with different contents of Y_2O_3. ODS-RHEAs are all composed of the matrix phase (light gray area) and dispersed particles (dark-gray and black areas). With the increase in Y_2O_3 content, the volume fraction of the particles gradually increases. The particle sizes of the black particles are in the range of $\sim$ 100 to 600 nm, while the dark-gray particles have a nano-size. According to EDS results, the black particle is composed of Ti (52.15 at%), N (21.77 at%), and O (22.85 at%), confirming that these black particles are Ti-(N, O) compounds. The nano-sized particles are too small to be identified in SEM analysis, and it will be analyzed by HRTEM later. In XRD patterns of bulk RHEAs (Fig. 2d), it can be seen that the bulk alloys have a similar phase constitution to the as-milled powders, suggesting that there is no new phase formed during the sintering.

Figure 3 shows EBSD results of NbTaTiV RHEAs with different contents of Y_2O_3. It can be seen from the inverse pole figures (IPF) that the average grain size gradually decreases as Y_2O_3 content increases from 1 wt% to 3 wt%, and the average grain size is determined to be 0.78, 0.73 and 0.64 μm, respectively. In addition, the phase maps also confirm that the ODS-RHEAs are mainly composed of BCC matrix phase and Ti-(N, O) phases, and the volume fraction of Ti-(N, O) phase increases from 4.3% to 8.1% with the Y_2O_3 content increasing from 1 wt% to 3 wt%. The nano-sized in situ formed Y-Ti-O particles and Y_2O_3 particles were not detected due to the insufficient resolution of EBSD detector. The inhomogeneous distribution of

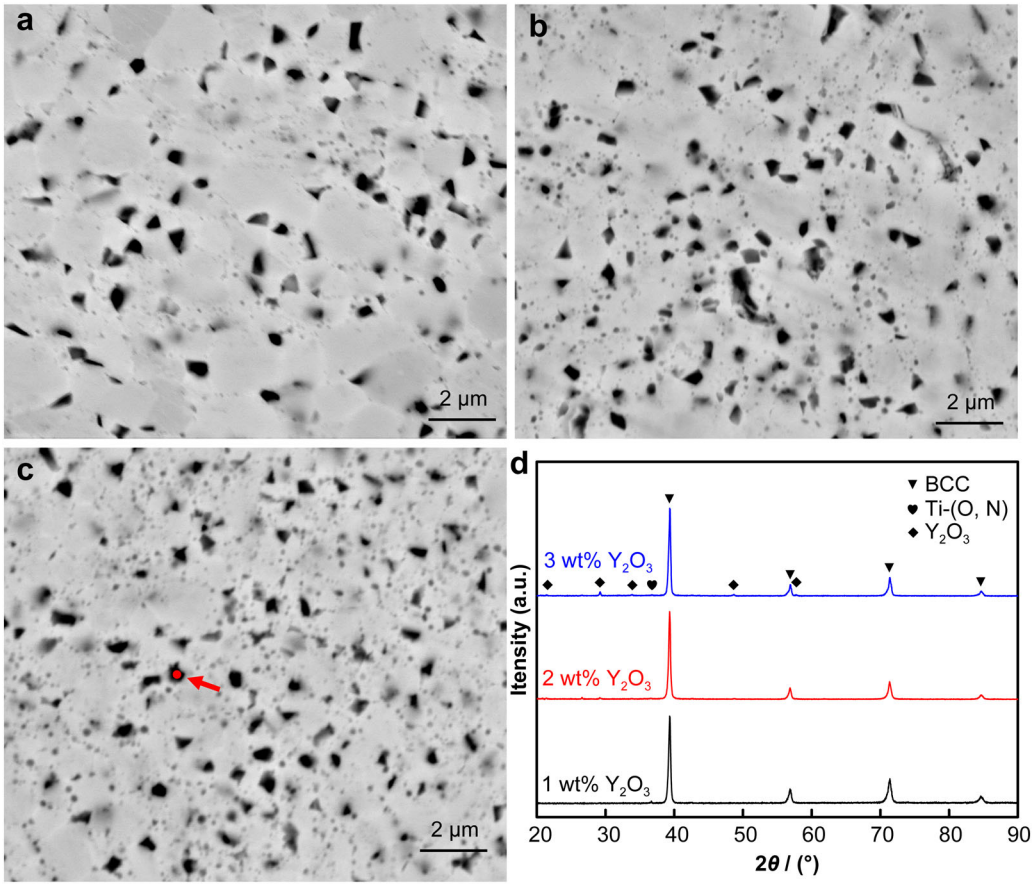

Fig. 2 **a–c** BSE images and **d** XRD patterns of bulk NbTaTiV RHEAs with different contents of Y_2O_3: **a** 1 wt% Y_2O_3; **b** 2 wt% Y_2O_3; **c** 3 wt% Y_2O_3

grains can be found from EBSD mappings, and many coarse grains can be detected and are decreased with Y_2O_3 content increasing. The phase diagram confirms that the Ti-(N, O) particles are mainly concentrated in the fine-grained region, and no particles are in the coarse-grained region, which is mainly because Ti-(N, O) particles can inhibit the rapid growth of grains at high sintering temperatures [18].

Figure 4a, b shows TEM image and size distribution of the particles in NbTaTiV RHEA with 3 wt% Y_2O_3. Two kinds of particles can be observed in TEM image, and those are ultrafine particles with particle size of lower than 25 nm and relatively coarse particles with particle size of higher than 100 nm. The average particle size is about 18.02 nm, and the majority of the particles are below 25 nm. Figure 4c, d shows selected area electron diffraction (SAED) patterns of the coarse particle (Point 1 in Fig. 4a) and the matrix (Point 2 in Fig. 4a). The results show that the coarse particles with submicron size have an FCC structure with a lattice constant of 0.4210 nm. Note that the lattice constants of TiO and TiN are 0.4177 and 0.4242 nm, respectively; therefore, these submicron particles can be determined to be Ti-(N, O) compounds, which agrees with the results in SEM analysis. In addition, the matrix has a BCC structure with a lattice constant of 0.3229 nm, which is similar to the lattice constant of the NbTaTiV RHEA (0.3230 nm) mentioned in our previous work [22].

To further understand the microstructure of the nano-sized particles in RHEAs, a HRTEM was used, and the results are shown in Fig. 5. The inserted images in the upper right corner are corresponding fast Fourier transform (FFT) results. HRTEM images and FFT results in Fig. 5a, b suggest that these particles could be $Y_2Ti_2O_7$ particles with a cubic structure. The average particle size is about 8 nm. The interplanar distances $d_{(331)P}$ of the particles in Fig. 5a, b are 0.2287 and 0.2280 nm, respectively, which are close to that of the matrix (0.2286 nm), suggesting that the interface between the particles and the matrix is coherent. Figure 5c, d shows HRTEM images of bigger particles, and (insets) corresponding FFT results. As shown, these bigger particles have a Y_2O_3 monoclinic structure, which suggests that these particles are excessive Y_2O_3 particles. The interfaces between the Y_2O_3 particles and the matrix are clearly non-coherent.

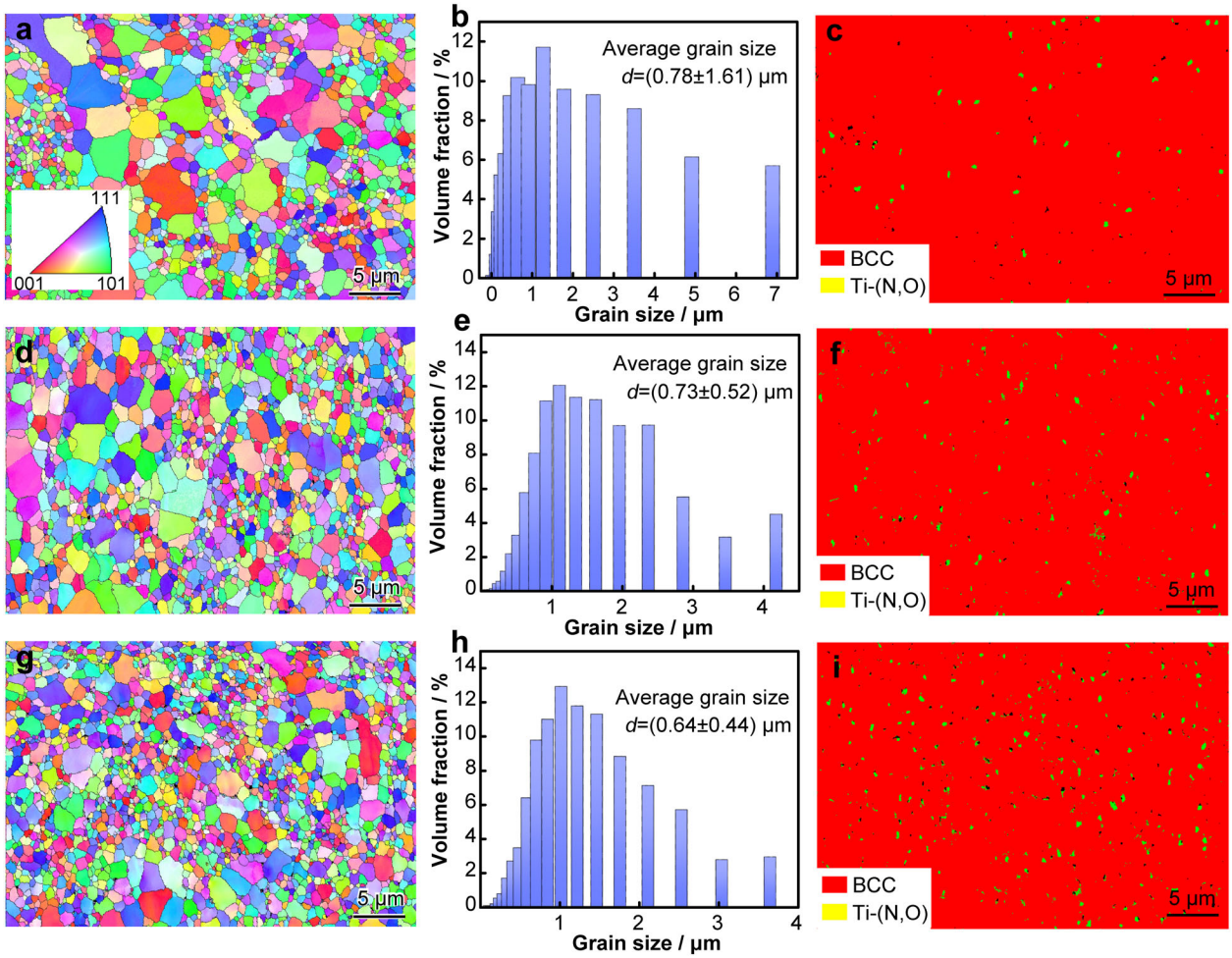

Fig. 3 EBSD IPF maps and grain size distributions of NbTaTiV RHEAs with different contents of Y_2O_3: **a–c** 1 wt% Y_2O_3; **d–f** 2 wt% Y_2O_3; **g–i** 3 wt% Y_2O_3

3.3 Effect of Y_2O_3 content on mechanical properties

Figure 6 presents Vickers microhardness of the NbTaTiV RHEAs with different contents of Y_2O_3. The microhardness values of the NbTaTiV RHEAs prepared by casting [5] and powder metallurgy [22] are also given, as plotted in the dotted line in Fig. 6. The hardness values of these ODS-NbTaTiV RHEAs are HV 466.7, HV 508.9 and HV 515.4, respectively, which are significantly higher than those of NbTaTiV RHEA prepared by casting (∼ HV 298) and powder metallurgy (∼ HV 427.9). The increase in hardness may be mainly related to the multiscale oxide particles.

Figure 7a shows compressive engineering stress–strain curves of the ODS-NbTaTiV RHEAs at room temperature. In our previous work [22], the yield strength, fracture strength and fracture strain of the NbTaTiV RHEA are 1108 MPa, 1821 MPa and 25%, respectively. In this study, the increase in the Y_2O_3 content leads to an obvious enhancement in mechanical properties. The ODS-NbTaTiV RHEA with 3 wt% Y_2O_3 has a yield strength of 1866 MPa, which is 68.4% higher than that of the NbTaTiV RHEA while maintaining a reasonable fracture strain of about 16%. Figure 7b gives the compressive yield strength and fracture strain of the present ODS-NbTaTiV RHEAs and some typical RHEAs [3–8, 22–25]. It can be clearly seen that the ODS-NbTaTiV RHEAs exhibit superior yield strength and fracture strength, which are better than most of the RHEAs and RHEA-based composites in the literature. Table 1 summarizes the compressive properties of several RHEAs and RHEA-based composites in the present study and literature [3–8, 22–26]. For example, the yield strength of the ODS-NbTaTiV RHEA with 3 wt% Y_2O_3 is 1866 MPa, which is obviously higher than those of the typical HfNbTaTiV RHEA [6], MoNbTaTiV RHEA [7] and the NbTaTiV [8]-based composites reinforced with Ti-C-O ceramic particles. Besides, the ODS-NbTaTiV RHEA with 3 wt% Y_2O_3 maintains a reasonable fracture strain of 16%.

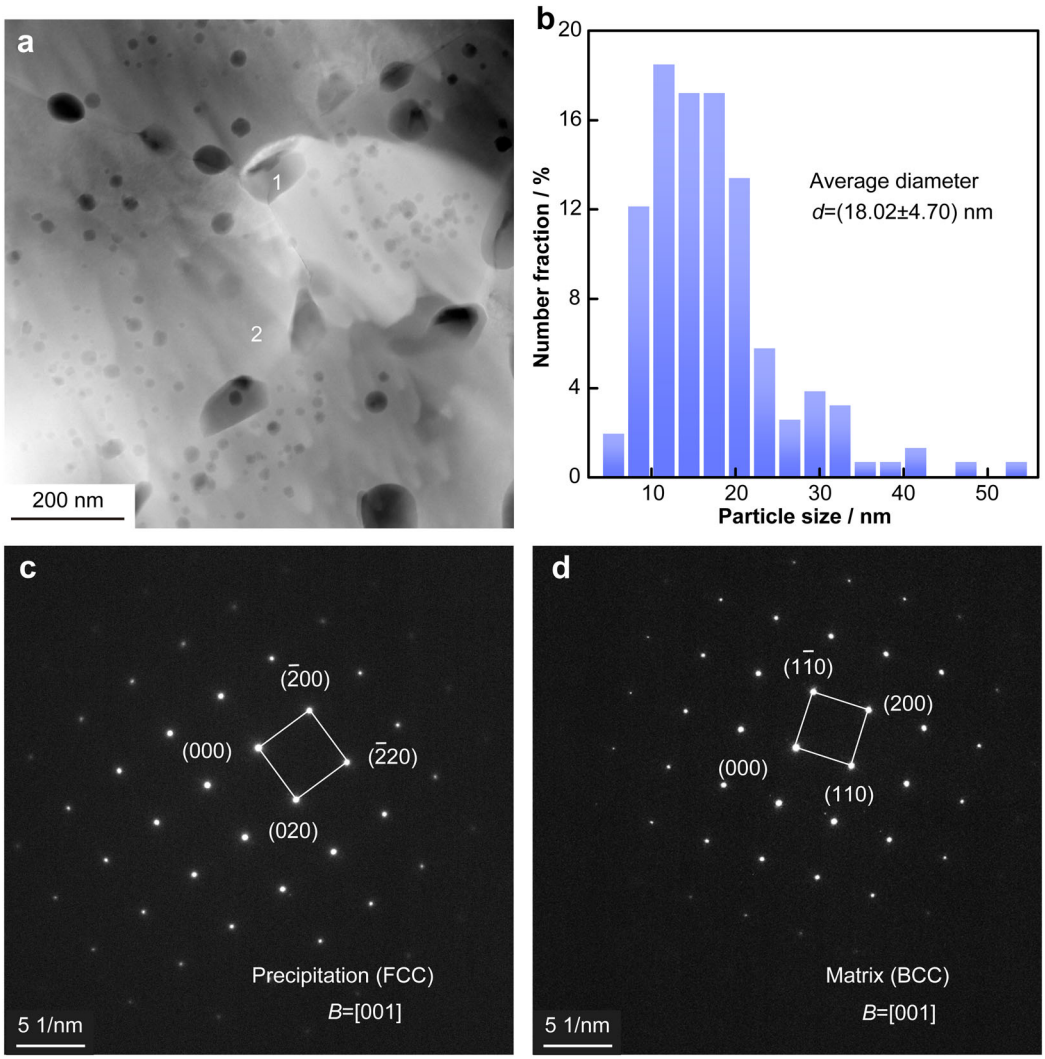

Fig. 4 **a** TEM image of nano-sized particles in NbTaTiV RHEA reinforced with 3 wt% Y_2O_3; **b** size distribution of particles; **c** SAED pattern of submicron particles; **d** SAED pattern of matrix

Figure 8 shows the fracture morphologies of the ODS-NbTaTiV RHEAs after compression tests. It is shown that all the ODS-NbTaTiV RHEAs exhibit typical intergranular fracture characteristics, which is related to the inherent brittleness of the BCC crystal structure. At the same time, from the high-magnified fracture images shown in Fig. 8d–f, it can be found that some holes with a size of around 300 nm are shown on the fracture surface, which may be caused by the pull-out effect of Ti-(N, O) particles during the deformation.

So far, many strengthening mechanisms have been proposed to evaluate the strength contribution of HEAs [9, 10, 27]. In this work, since the RHEAs have added a predetermined amount of nano-sized oxides, the remarkable mechanical properties of the ODS-NbTaTiV RHEAs are mainly related to the strengthening of multiscale oxides, including the submicron Ti-(N, O) particles, the nano-sized Y-Ti-O particles, and the nano-sized Y_2O_3 particles [28, 29]. Besides, grain boundary strengthening caused by refined grains also partly contributes to enhanced mechanical properties [10]. As for particle strengthening, usually, the dislocation by-pass mechanism occurs when the particles are large enough (usually several tens of nanometers or more) and incoherent with the matrix, and the shearing mechanism would dominate when particles are sufficiently small or coherent with the matrix. In this study, the submicron Ti-(N, O) particles and the nano-sized Y_2O_3 particles have a non-coherent interface with the BCC matrix, thereby mainly strengthening the ODS-RHEAs through the dislocation by-pass mechanism [30, 31]. However, the nano-sized Y-Ti-O particles exhibit a coherent interface with BCC matrix, therefore mainly strengthening the ODS-RHEAs through the

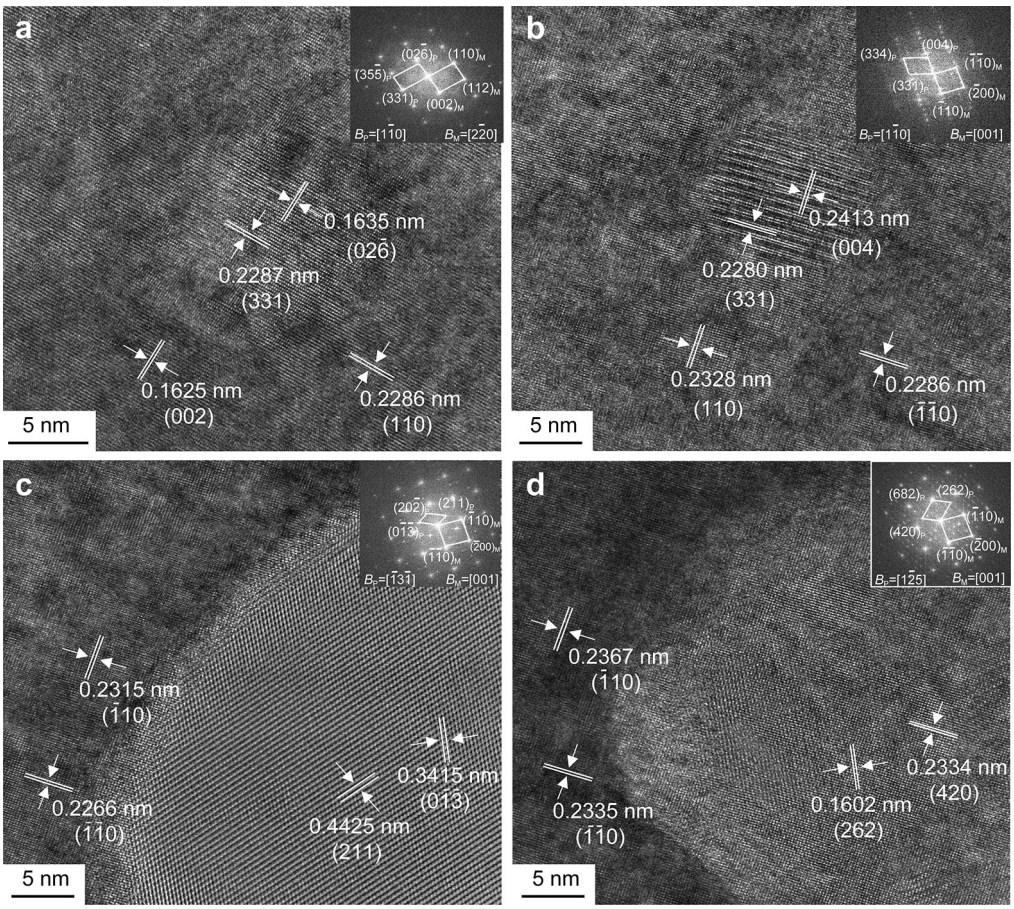

Fig. 5 HRTEM images of nano-sized particles and their corresponding FFT images of NbTaTiV RHEA with 3 wt% Y_2O_3: **a, b** Y-Ti-O particles; **c**, **d** Y_2O_3 particles (noting that P is for particle and M is for matrix in FFT images)

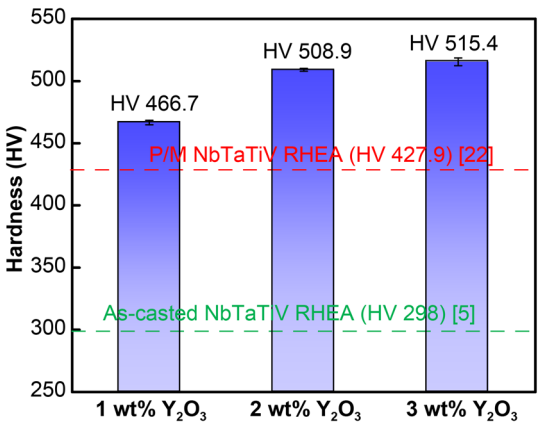

Fig. 6 Vickers microhardness of NbTaTiV RHEAs with different contents of Y_2O_3 and NbTaTiV RHEAs prepared by casting [5] and powder metallurgy [22]

dislocation shearing mechanism [9]. Therefore, the enhanced strength from the dispersed oxide particles can be estimated as the sum of several strengthening mechanisms and expressed as:

$$\Delta\sigma = \Delta\sigma_{\mathrm{D}} + \Delta\sigma_{\mathrm{P}} \tag{1}$$

where $\Delta\sigma_{\mathrm{D}}$ and $\Delta\sigma_{\mathrm{P}}$ are the dispersion strengthening caused by nanoscale Y-Ti-O particles and precipitation strengthening caused by submicron Ti-(N, O) particles. To simplify the calculation, Y_2O_3 particles are not taken into account in the above calculation due to their small volume fraction. The dispersion strengthening can be evaluated by the Seeger model [32, 33], as follows:

$$\Delta\sigma_{\mathrm{D}} = 0.8M\alpha(r)Gb/\lambda \tag{2}$$

where M is the Taylor factor of the BCC structure [18]; G and b are the shear modulus and Burman's vector of the base alloy, respectively [5]; λ is the average distance between particles, which is given by Eq. (3) [31]; $\alpha(r)$ is the barrier strength coefficient of the particles, which is given by Eq. (4) [33]:

$$\lambda = 2\sqrt{\frac{2}{3}}r\left(\left(\frac{\pi}{4f}\right)^{1/2} - 1\right) \tag{3}$$

where f and r are the volume fraction and average particle size of the Y-Ti-O, respectively.

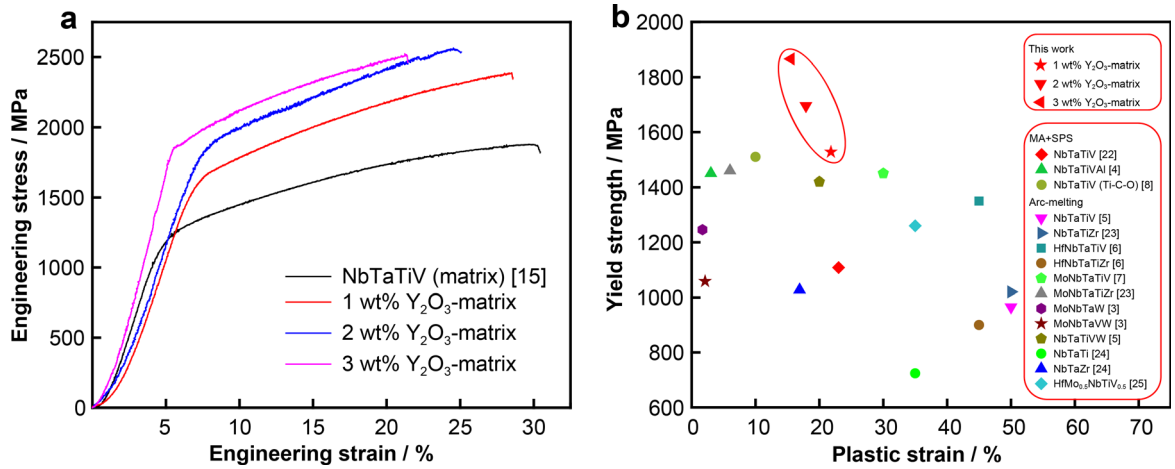

Fig. 7 **a** Room-temperature compressive engineering stress–strain curves of NbTaTiV RHEAs with different contents of Y_2O_3; **b** comparison of compressive yield strength and plastic strain of this work and some typical RHEAs

Table 1 Room-temperature compressive properties of several RHEAs in present study and literature

Materials	Preparation methods	Phase structure	Yield strength / MPa	Ultimate strength / MPa	Plastic fracture strain / %	Refs.
1 wt%-NbTaTiV	MA + SPS	BCC	1528	2389	22.0	This work
2 wt%-NbTaTiV	MA + SPS	BCC	1696	2560	18.0	This work
3 wt%-NbTaTiV	MA + SPS	BCC	1866	2523	16.0	This work
NbTaTiV	MA + SPS	BCC	1108	1821	~ 23.0	[22]
NbTaTiVAl	MA + SPS	BCC	1450	1619	~ 3.0	[4]
NbTaTiV/Ti-C-O	MA + SPS	BCC	1510	– 2050	~ 10.0	[8]
NbTaTiV	Arc-melting	BCC	965	– 1370	50.0	[5]
NbTaTiZr	Arc-melting	BCC	1020	–	50.0	[23]
HfNbTaTiV	Arc-melting	BCC	1350	–	> 45.0	[6]
HfNbTaTiZr	Arc-melting	BCC	900	–	> 45.0	[6]
MoNbTaTiV	Arc-melting	BCC	1400	2450	30.0	[7]
MoNbTaTiZr	Arc-melting	BCC	1460	– 1750	6.0	[23]
MoNbTaW	Arc-melting	BCC	1246	1270	1.7	[3]
MoNbTaVW	Arc-melting	BCC	1058	1211	2.1	[3]
NbTaTiVW	Arc-melting	BCC	1420	– 1880	20.0	[5]
NbTaVW	Arc-melting	BCC	1530	– 1700	12.0	[5]
NbTaTi	Arc-melting	BCC	724	1137	> 35.0	[24]
NbTaZr	Arc-melting	BCC	1027	1409	16.9	[24]
$HfMo_{0.5}NbTiV_{0.5}$	Arc-melting	BCC	1260	–	> 35.0	[25]
HfMoTaTiZr	Arc-melting	BCC	1600	– 1750	4.0	[26]

$$\alpha(r) = -0.017 + 0.374\lg(r/2b) \tag{4}$$

where $\alpha(r)$ represents the impeding ability of dislocation movement from the particles. When the value of $\alpha(r)$ is very small, the particles appear as a soft barrier, and the strengthening effect mainly comes from the dislocation shearing mechanism [34, 35]. When the value of $\alpha(r)$ is large (≥ 1), the strengthening effect will turn to be the dislocation by-pass mechanism [36]. Therefore, the precipitation strengthening caused by Ti-(N, O) precipitates is more suitable to be calculated by the Orowan model [9, 30], expressed as follows:

$$\Delta\sigma_P = M\frac{0.4Gb}{\pi\lambda}\cdot\frac{\ln(2\bar{r}/b)}{(1-v)^{1/2}} \tag{5}$$

where $\bar{r} = \sqrt{2/3}r$, and v is the Poisson's ratio of the matrix alloy [19].

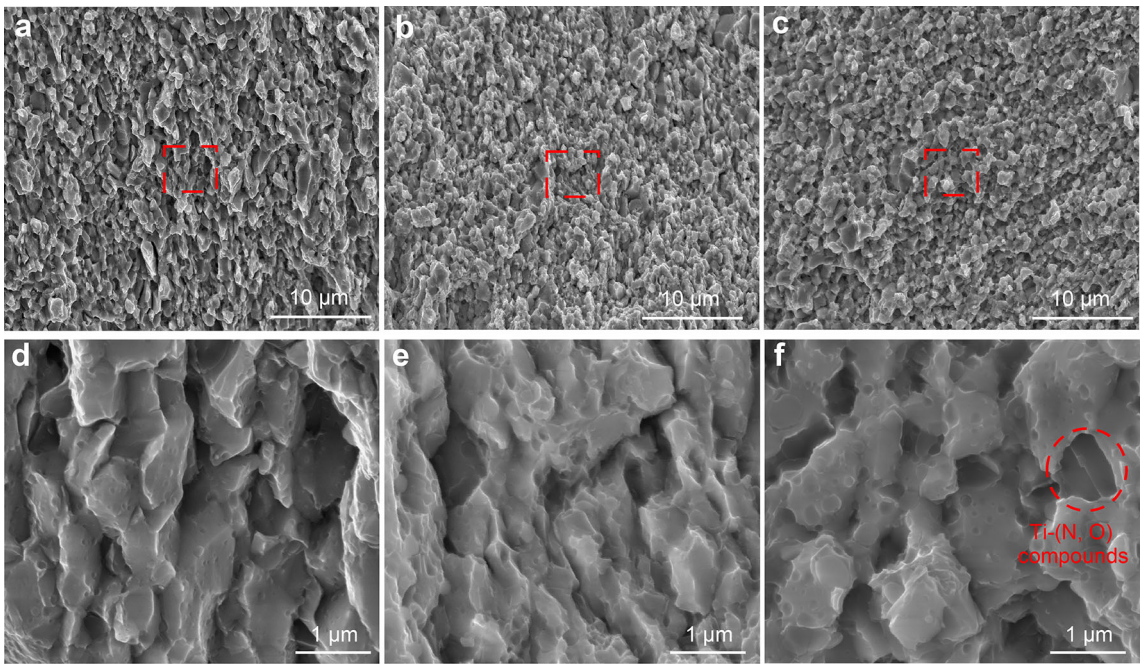

Fig. 8 Fracture morphologies of NbTaTiV RHEAs with different contents of Y_2O_3: **a, d** 1 wt% Y_2O_3; **b, e** 2 wt% Y_2O_3; **c, f** 3 wt% Y_2O_3

Table 2 Various strengthening mechanisms and parameters used to calculate strengthening mechanism

Strengthening mechanism	Symbol	Parameter	Value
Dispersion strengthening:$\Delta\sigma_D = 0.8M\alpha(r)Gb/\lambda$	M	Taylor factor	2.9
	r / nm	Average particle radius	9.01
	f / %	Mean volume fraction	6.215
	α / r	Obstacle strength coefficient	0.466
	G / GPa	Shear modulus	52.025
	b / nm	Burgers vector	0.25
	λ / nm	Inter-precipitate spacing	37.58
Precipitation strengthening:$\Delta\sigma_{or} = M\frac{0.4Gb}{\pi\lambda}\cdot\frac{\ln(2\bar{r}/b)}{(1-\nu)^{1/2}}$	$\bar{r}$ / nm	Average radius	143.80
	f / %	Mean volume fraction	9.45
	λ / nm	Inter-precipitate spacing	442.15
	ν	Poisson's ratio	0.358

Table 2 gives the values of corresponding parameters in the above discussion. Based on the given parameters and the strengthening models, the dispersion strengthening ($\Delta\sigma_D$) and precipitation strengthening ($\Delta\sigma_P$) of the ODS-NbTaTiV RHEA with 3 wt% Y_2O_3 were determined to be 344.38 and 86.44 MPa, respectively. In summary, it can be deduced that the enhanced yield strength of the ODS RHEAs is mainly ascribed to the in situ formed nanoscale Y-Ti-O precipitates and submicron Ti-(N, O) particles.

Moreover, with the increase in Y_2O_3 content, both the yield strength and fracture strength of the ODS-NbTaTiV RHEAs increase gradually. This can be attributed to several effects. First, the increase in Y_2O_3 content leads to an increased amount of in situ formed Ti-(N, O) and Y-Ti-O particles, thereby leading to further particle strengthening. Second, with Y_2O_3 content increasing, the excessive Y_2O_3 particles could also strengthen the ODS-NbTaTiV RHEAs. Besides, the grain is gradually refined with the increase in Y_2O_3 addition, which also contributes to the increase in strength. Therefore, a superior mechanical property is achieved in the ODS-NbTaTiV RHEAs.

4 Conclusion

A new ODS-NbTaTiV RHEA with multiscale ultrafine particles was successfully developed through MA and SPS methods. In these RHEAs, the introduction of Y_2O_3 particles can lead to the in situ formation of the submicron Ti-(N, O) particles and nano-sized Y-Ti-O particles and also cause grain refining in the matrix. The novel ODS-NbTaTiV RHEAs exhibit superior mechanical properties compared with most of the RHEAs and RHEA-based composites. The yield strength and fracture strength of the ODS-NbTaTiV RHEA with 3 wt% Y_2O_3 are 1866 and 2523 MPa, respectively, which are 68.4% and 38.6% higher than that of the NbTaTiV matrix alloy. The enhanced mechanical properties of the ODS-NbTaTiV RHEAs are mainly attributed to the multiscale oxide dispersion strengthening from the submicron Ti-(N, O) particles, nano-sized Y-Ti-O particles and Y_2O_3 particles, and the grain boundary strengthening from ultrafine grain structure.

Acknowledgements This study was financially supported by the National Natural Science Foundation of China (Nos. 51771232 and 52104365).

Declarations

Conflict of interests The authors declare that they have no conflict of interest.

References

[1] Chen J, Zhou X, Wang W, Liu B, Lv Y, Yang W, Xu D, Liu Y. A review on fundamentals of high entropy alloys with promising high-temperature properties. J Alloy Compd. 2018;760:15.
[2] Senkov ON, Wilks GB, Miracle DB, Chuang CP, Liaw PK. Refractory high-entropy alloys. Intermetallics. 2010;18(9):1758.
[3] Senkov ON, Wilks GB, Scott JM, Miracle DB. Mechanical properties of $Nb_{25}Mo_{25}Ta_{25}W_{25}$ and $V_{20}Nb_{20}Mo_{20}Ta_{20}W_{20}$ refractory high entropy alloys. Intermetallics. 2011;19(5):698.
[4] Xiang L, Guo WM, Liu B, Fu A, Li J, Fang QH, Liu Y. Microstructure and mechanical properties of $TaNbVTiAl_x$ refractory high-entropy alloys. Entropy. 2020;22(3):282.
[5] Yao HW, Qiao JW, Gao MC, Hawk JA, Ma SG, Zhou HF, Zhang Y. NbTaV-(Ti, W) refractory high-entropy alloys: experiments and modeling. Mat Sci Eng A. 2016;674:203.
[6] An Z, Mao S, Liu Y, Wang L, Zhou H, Gan B, Zhang Z, Han X. A novel HfNbTaTiV high-entropy alloy of superior mechanical properties designed on the principle of maximum lattice distortion. J Mater Sci Technol. 2021;79:109.
[7] Yao HW, Qiao JW, Hawk JA, Zhou HF, Chen MW, Gao MC. Mechanical properties of refractory high-entropy alloys: experiments and modeling. J Alloy Compd. 2017;696:1139.
[8] Fu A, Guo WM, Liu B, Cao YK, Xu L, Fang QH, Yang H, Liu Y. A particle reinforced NbTaTiV refractory high entropy alloy-based composite with attractive mechanical properties. J Alloy Compd. 2020;815: 152466.
[9] Gwalani B, Pohan RM, Waseem OA, Alam T, Hong SH, Ryu HJ, Banerjee R. Strengthening of $Al_{0.3}$CoCrFeMnNi-based ODS high entropy alloys with incremental changes in the concentration of Y_2O_3. Scr Mater. 2019;162:477.
[10] Rao KR, Sinha SK. Effect of sintering temperature on microstructural and mechanical properties of SPS processed CoCrCuFeNi based ODS high entropy alloy. Mater Chem Phys. 2020;256:123709.
[11] Peng S, Lu Z, Yu L. Effects of Y_2O_3/Ti/Zr addition on microstructure and hardness of ODS-CoCrFeNi HEAs produced by mechanical alloying and spark plasma sintering. J Alloy Compd. 2021;861:157940.
[12] Liu Y, Zhang YA, Wang W, Li DS, Ma YJ. Influence of rare earth Y on microstructure and high temperature oxidation behavior of Ni-Fe-Co-Cu alloy. Chin J Rare Met. 2020;44(1):9.
[13] El-Genk MS, Tournier JM. A review of refractory metal alloys and mechanically alloyed-oxide dispersion strengthened steels for space nuclear power systems. J Nucl Mater. 2005;340(1):93.
[14] Gwalani B, Pohan RM, Lee J, Lee B, Banerjee R, Ryu HJ, Hong SH. High-entropy alloy strengthened by in situ formation of entropy-stabilized nano-dispersoids. Sci Rep-UK. 2018;8:14085.
[15] Prasad H, Singh S, Panigrahi BB. Mechanical activated synthesis of alumina dispersed FeNiCoCrAlMn high entropy alloy. J Alloy Compd. 2017;692:720.
[16] Hadraba H, Chlup Z, Dlouhy A, Dobes F, Roupcova P, Vilemova M, Matejicek J. Oxide dispersion strengthened CoCrFeNiMn high-entropy alloy. Mat Sci Eng A. 2017;689:252.
[17] Gao N, Long Y, Peng H, Zhang W, Peng L. Microstructure and mechanical properties of TiVNbTa refractory high-entropy alloy prepared by powder metallurgy. Chin J Mater Res. 2019;33(8):572.
[18] Liu Q, Wang G, Sui X, Liu Y, Li X, Yang J. Microstructure and mechanical properties of ultra-fine grained MoNbTaTiV refractory high-entropy alloy fabricated by spark plasma sintering. J Mater Sci Technol. 2019;35(11):2600.
[19] Liu Q, Wang G, Sui X, Xu Y, Liu Y, Yang J. Ultra-fine grain Ti_xVNbMoTa refractory high-entropy alloys with superior mechanical properties fabricated by powder metallurgy. J Alloy Compd. 2021;865:158592.
[20] Ressel G, Holec D, Fian A, Mendez-Martin F, Leitner H. Atomistic insights into milling mechanisms in an Fe–Y_2O_3 model alloy. Appl Phys A. 2014;115:851.
[21] Wu Y, Zhao HZ, Li JK, Zhang YY, Liu T. Effects of $Y_4Zr_3O_{12}$ addition on the microstructure and mechanical properties of Fe–15Cr–2W-0.35Ti ODS steels. Mat Sci Eng A. 2021;804:140734.
[22] Guo WM, Liu B, Liu Y, Li T, Fu A, Fang QH, Nie Y. Microstructures and mechanical properties of ductile NbTaTiV refractory high entropy alloy prepared by powder metallurgy. J Alloy Compd. 2019;776:428.
[23] Wang SP, Xu J. (TiZrNbTa)-Mo high-entropy alloys: dependence of microstructure and mechanical properties on Mo concentration and modeling of solid solution strengthening. Intermetallics. 2018;95:59.
[24] Senkov ON, Gild J, Butler TM. Microstructure, mechanical properties and oxidation behavior of NbTaTi and NbTaZr refractory alloys. J Alloy Compd. 2021;862: 158003.
[25] Juan CC, Tsai MH, Tsai CW, Lin CM, Wang WR, Yang CC, Chen SK, Lin SJ, Yeh JW. Enhanced mechanical properties of HfMoTaTiZr and HfMoNbTaTiZr refractory high-entropy alloys. Intermetallics. 2015;62:76.
[26] Liu Y, Zhang Y, Zhang H, Wang N, Chen X, Zhang H, Li Y. Microstructure and mechanical properties of refractory $HfMo_{0.5}NbTiV_{0.5}Si_x$ high-entropy composites. J Alloy Compd. 2017;694:869.

[27] Yao HW, Qiao JW, Gao MC, Hawk JA, Ma SG, Zhou HF. MoNbTaV medium-entropy alloy. J Mater Sci Technol Entropy. 2016;18(5):189.
[28] Yang L, Ryutan C, Zheng Y, Mohammad HSB, Abdul R, Zhang C, Chen H, Yang ZG. Spalling resistance of thermally grown oxide based on NiCoCrAlY(Ti) with different oxide peg sizes. Rare Met. 2021;40(3):663.
[29] Hu YM, Liu XD, Guo NN, Wang L, Su YQ, Guo JJ. Microstructure and mechanical properties of NbZrTi and NbHfZrTi alloys. Rare Met. 2019;38(9):840.
[30] Cao YK, Zhang WD, Liu B, Liu Y, Du M, Fu A. Phase decomposition behavior and its effects on mechanical properties of $TiNbTa_{0.5}ZrAl_{0.5}$ refractory high entropy alloy. J Mater Sci Technol. 2021;66:10.
[31] Wen H, Topping TD, Isheim D, Seidman DN, Lavernia EJ. Strengthening mechanisms in a high-strength bulk nanostructured Cu-Zn-Al alloy processed via cryomilling and spark plasma sintering. Acta Mater. 2013;61(8):2769.
[32] Seeger A. On the theory of radiation damage and radiation hardening. Proc 2nd UN Int Conf on Peaceful Uses of Atomic Energy. Geneva; 1958.6.
[33] Alinger MJ, Odette GR, Hoelzer DT. On the role of alloy composition and processing parameters in nanocluster formation and dispersion strengthening in nanostructured ferritic alloys. Acta Mater. 2009;57(2):392.
[34] Wu Y, Liaw PK, Zhang Y. Preparation of Bulk TiZrNbMoV and NbTiAlTaV high-entropy alloys by powder sintering. Metals. 2021;11(11):1748.
[35] Zhang S, Wang Z, Yang HJ, Qiao JW, Wang ZH, Wu YC. Ultra-high strain-rate strengthening in ductile refractory high entropy alloys upon dynamic loading. Intermetallics. 2020;121:106699.
[36] Guo Y, Li M, Chen C, Li P, Li W, Ji Q, Zhang Y, Chang Y. Oxide dispersion strengthened FeCoNi concentrated solid-solution alloys synthesized by mechanical alloying. Intermetallics. 2020;117: 106674.